applied sciences

MDPI

Article

Water Basin Effect of Cofferdam Foundation Pit

Guofeng Li [1,2,*], Qinchao Zuo [3], Xiaoyan Zhou [3], Yanbo Hu [4] and Ning Li [4]

[1] State Key Laboratory of Eco-Hydraulics in Northwest Arid Region of China, Xi'an University of Technology, Xi'an 710048, China
[2] Shaanxi Provincial Institute of Water Resources and Electric Power Investigation and Design, Xi'an 710000, China
[3] Shaanxi Institute of Engineering Investigation Co., Ltd., Xi'an 710068, China
[4] School of Civil and Architectural Engineering, Xi'an University of Technology, Xi'an 710048, China; hybafi@163.com (Y.H.); ningli@xaut.edu.cn (N.L.)
* Correspondence: liguofeng205@126.com

Abstract

This study addresses the water basin effect in the underwater sand layer of steel pipe pile cofferdams by integrating the concept from building foundation pits to cofferdam foundation pit analysis. A theoretical derivation is presented for the deformation evolution of steel pipe piles and bottom seals within the cofferdam pit. The cofferdam construction dewatering process is divided into four stages: riverbed excavation for bottom sealing, dewatering to the second support, dewatering to the third support, and dewatering to final bottom sealing. The steel pipe piles are modeled as single-span or multi-span cantilever continuous beam structures. Using the superposition principle, deformation evolution equations for these statically indeterminate structures across the four stages are derived. The bottom seal is simplified to a single-span end-fixed beam, and its deflection curve equation under uniform load and end-fixed additional load is obtained via the same principle. A case study based on the 6# pier steel pipe pile cofferdam of Xi'an Metro Line 10 Jingwei Bridge rail-road project employs FLAC3D for hydrological–mechanical coupling analysis of the entire dewatering process to validate the water basin effect. Results reveal a unique water basin effect in cofferdam foundation pits. Consistent horizontal deformation patterns of steel pipe piles occur across all working conditions, with maximum horizontal displacement (20.72 mm) observed at 14 m below the pile top during main pier construction completion. Close agreements are found among theoretical, numerical, and monitored deformation results for both steel pipe piles and bottom seals. Proper utilization of the formed water basin effect can effectively enhance cofferdam stability. These findings offer insights for similar engineering applications.

Keywords: water basin effect; deformation evolution mechanism; steel pipe pile cofferdam; hydrological–mechanical coupling

Academic Editor: Tiago Filipe da Silva Miranda

Received: 10 May 2025
Revised: 19 June 2025
Accepted: 24 June 2025
Published: 30 June 2025

Citation: Li, G.; Zuo, Q.; Zhou, X.; Hu, Y.; Li, N. Water Basin Effect of Cofferdam Foundation Pit. *Appl. Sci.* **2025**, *15*, 7374. https://doi.org/10.3390/app15137374

1. Introduction

The construction of large-span bridge bearing platforms presents significant challenges, including demanding foundation pit excavation, heightened risks of base uplift, critical requirements for secure cofferdam embedment, and susceptibility of mass concrete to cracking [1]. Among these, river-crossing bridge pier cofferdams are particularly crucial for constructing underwater foundations. Cofferdams serve as indispensable temporary structures across diverse domains such as hydrological engineering [2], municipal infrastructure [3], transportation engineering [4], ocean engineering [5,6], port construction [7,8],

waterway projects [9], and ecological engineering [10]. Their primary function is to isolate construction zones from water ingress, thereby creating dry working environments [11]. Continuous advancements in engineering technology, integrating novel materials and methodologies, progressively enhance cofferdam efficiency and safety.

Alongside the sustained development of China's infrastructure capabilities, the proliferation of river- and sea-crossing bridges has stimulated substantial research on pier cofferdams [12–14]. Key research areas encompass innovative cofferdam configurations [4], structural optimization [15], structural responses during construction phases [16], and stability under extreme loading conditions [5,17], contributing significantly to advancements in China's water-crossing bridge engineering.

Existing studies predominantly employ numerical simulations, model tests, and in situ monitoring to analyze the effects of construction sequences [16], loading scenarios, enclosure structure designs, and stratum properties [18] on cofferdam deformation, stress distribution, and stability. Kai & Wang investigated mechanical properties, deformation characteristics, and design optimization based on actual foundation pit construction procedures, integrating numerical simulation with on-site monitoring [15,19]. Chen analyzed cofferdam deformation and structural behavior using the principle of equivalent bending stiffness, while detailed numerical simulations examined the influence of parameters such as pile length, dam width, tie rod spacing, and pile spacing [20]. Novel methods simulating penetration processes, accounting for deformation in slender profiles with low bending and torsional stiffness, have been developed and validated via model tests [21]. Li explored internal deformation mechanisms within double-row pile anti-sliding systems, using numerical simulations and transparent soil model tests to investigate the influence of section shape, row spacing, and pile layout on soil-arching effect formation, development, and failure [22]. Shen developed physical and numerical models to study how short rear piles affect earth pressure evolution in stabilized soil [23], while Hui's research addressed the bearing capacity of double-row steel sheet piles based on reinforcement depth and inter-pile soil properties [24]. Some studies have formulated multi-objective optimization models to address the lack of systematic, practical evaluation frameworks for selecting steel pipe pile cofferdam construction schemes [4]. Lu investigated failure mechanisms of nonuniform geotextile-reinforced cofferdams under seepage and excavation on soft sediments [25]. Li demonstrated that spatial heterogeneity and degradation of soil properties also significantly impact cofferdam stability in soft soil foundations [26]. However, there is still a lack of theoretical analysis research on the essential characteristics of the stress and deformation of the cofferdam structure system, especially the evolution theory of the stress and deformation during the cofferdam construction process of drain water, excavation, and support.

The cofferdam foundation pit needs to address not only its own structural and constructional effects [15,16,19] (including the stability of the cofferdam foundation pit itself, stress concentration, material fatigue, and additional impacts during construction and demolition), but also hydraulic effects [5,7,17] (such as changes in flow direction and velocity, local scouring and siltation, water level rise, and flood risks), geological and foundation effects [25,26] (including foundation settlement and displacement, seepage, and piping risks), as well as environmental and ecological effects (such as water quality and pollution, ecosystem disturbance, noise, and dust pollution). Hu integrated saturated–unsaturated seepage theory and strength reduction methods within finite element systems to analyze fluid–solid coupling stability and seepage failure during water-level fluctuations in dump-fill cofferdams [27]. Xu & Zhu utilized fluid dynamics methods to analyze the influence of external water flow characteristics on cofferdam deformation and stability [5,7]. Ti evaluated random wave pressure on sea-crossing bridge cofferdams under tropical cy-

clones using measured and numerical data [13]. Noh simulated flow field variations and scour depth around cofferdams using two-dimensional hydrodynamic analysis and bed-load transport models [28]. Chen & Jiang investigated seabed response around dumbbell cofferdams under combined wave-current loading [29], along with deformation characteristics and stability during super-historical floods, proposing emergency reinforcement strategies [17]. Other research numerically explores complex wave hydrodynamics under multidirectional extreme waves, systematically analyzing key factors including significant wave height, peak period, water depth, spreading angle, incident wave angle, and submergence depth [30]. However, these studies frequently overlook the influence of hydro-mechanical coupling characteristics on bottom-seal concrete deformation and rarely employ theoretical approaches to analyze cofferdam support structure system deformation. Bottom-sealing concrete placement is a pivotal construction phase, preventing hydraulic seepage and maintaining cofferdam structural equilibrium. The geometric dimensions and construction quality of this concrete layer profoundly impact its functionality. Determining an optimal thickness for bottom-sealing concrete under substantial hydraulic heads remains challenging, compounded by limited relevant investigations and a lack of consolidated theoretical frameworks [31]. Cofferdam stability is paramount for bridge construction safety, also requiring comprehensive consideration of hydrological parameters, geological conditions, and environmental protection requirements.

Under complex hydrodynamic conditions, steel-concrete composite single-wall caisson cofferdams may experience bottom-seal concrete leakage, internal support instability, or even structural collapse [32]. These issues persist as significant challenges in pier construction within deep sand layers, fundamentally stemming from the water basin effect [33]. However, few people deeply realize that the inherent mechanism and essence of deformation and failure of the cofferdam foundation pit is a problem of water bowl effect, and so, almost no one has particularly proposed and studied the water bowl effect problem unique to the cofferdam foundation pit. This effect significantly impacts the support structure system's mechanical behavior and stability. Although prior research has addressed seepage mechanisms [34,35], failure modes, and flood-control measures [23] via hydro-mechanical coupling analyses, the specific "water basin effect" within the steel pipe pile-bottom-seal concrete system formed after sealing in underwater sand layers remains inadequately explored.

Derived from the principle of buoyancy or Archimedes' principle, the water basin effect was initially proposed in the context of building foundation pits [33]. When the hydrostatic uplift force from the trapped water below the basement slab surpasses the total structural anti-uplift capacity, upward displacement and cracks of the basement occur. Subsequently, the effect was applied to analyze tunnel bed damage, where seepage water degrades the bed concrete, causing the unballasted track bed to float and bulge under the combined action of water pressure behind the lining, with damage occurring even at relatively low water heads [36].

While characterized in building foundation pits and tunnel beds, the manifestation and governing mechanisms of the water basin effect in cofferdam foundation pits require clarification. This study addresses this critical gap by introducing the water basin effect concept into cofferdam engineering based on a large number of numerical simulation experiments in the early stage [37,38]. The stress and deformation theoretical analysis of the simply supported beam under various loads [39], especially the triangular load acting in the middle of the span, is supplemented and perfected. The evolution characteristics of the stress and deformation of the steel pipe pile and the bottom seal are analyzed and derived by using the superposition method and the incremental method for the four typical stages during the construction of the cofferdam. Through theoretical derivations, combined

with FLAC3D 6.0 -based hydro-mechanical coupling simulations of the 6# pier cofferdam project for the Xi'an Metro Line 10 Jingwei River Rail-Road Bridge (China), and validation against in situ monitoring data, this work systematically elucidates the water basin effect mechanism and the evolution of steel pipe pile deformation in cofferdam foundation pits.

2. Principle of Cofferdam Foundation Pit Water Basin Effect

Archimedes' principle states that a body submerged in a fluid experiences an upward buoyant force equal to the weight of the displaced fluid. For subaqueous engineering structures, designers typically rely on the hydrostatic pressure at the design water level specified in geotechnical reports for anti-uplift design, often neglecting the structural safety risks induced by the "water basin effect" caused by surface water ingress or groundwater level fluctuations [33].

2.1. Water Basin Effect in Building Foundation Pits

The water basin effect in building foundation pits is defined as the phenomenon whereby insufficient backfill compaction allows surface, groundwater, and construction runoff to accumulate beneath the basement slab within an impermeable strata-confined zone (Figure 1). When the hydrostatic uplift force exerted by this trapped water exceeds the structural anti-uplift capacity-comprising self-weight and engineered countermeasures, the basement may experience upward displacement [40].

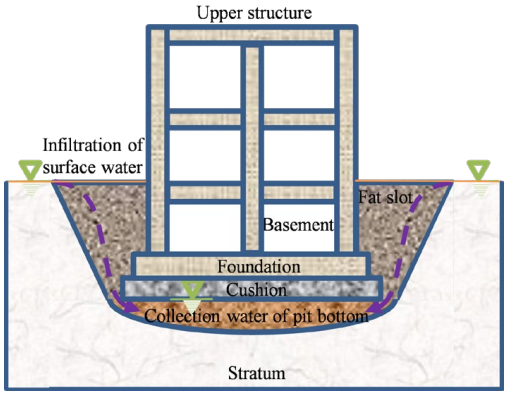

Figure 1. Schematic of water basin effect in building foundation pits.

This effect commonly induces construction defects, including basement slab heave, wall cracks, and beam–column joint fissures, primarily due to inadequate control of backfill permeability and compaction quality. Theoretically, properly compacted backfill should exhibit lower permeability than undisturbed soil; however, substandard construction disrupts this design intent. During heavy rainfall, surface water infiltrates the foundation pit through poorly compacted backfill zones, forming a confined water basin beneath the basement. The structure then acts as a "sub-basin" floating within this larger hydrological system: when buoyant forces surpass the sum of structural dead load and anti-uplift resistances, uplift failure occurs.

2.2. Water Basin Effect in Cofferdam Foundation Pits

Cofferdam foundation pits share analogous hydro-mechanical characteristics with building foundation pits, whereby the semi-infinite extra-cofferdam hydro-sedimentary environment constitutes a "macro-basin", while the post-sealing steel pipe piles and concrete bottom form a confined "micro-basin" floating within this macro-system (Figure 2). Structural instability occurs when hydraulic uplift forces exerted by the surrounding water exceed the combined dead load of the superstructure, leading to potential anti-uplift failures.

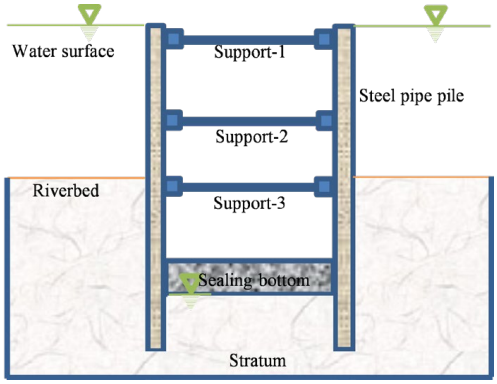

Figure 2. Schematic of water basin effect in cofferdam foundation pits.

Under the combined action of the water basin effect and differential hydro-sedimentary pressures across the cofferdam boundary, the bottom seal exhibits heightened uplift susceptibility even at relatively low hydraulic gradients. When rigidly connected to the cofferdam steel piles and subjected to significant pressure differentials, the central region of the bottom seal may undergo bulging deformation or even tensile cracking due to flexural stresses induced by confined water accumulation.

3. Deformation Evolution Mechanism of Cofferdam Foundation Pit

Following the placement of the bottom seal concrete, a coupled water basin effect involving steel pipe piles and the seal structure is induced. The steel piles, supported by internal braces and the bottom seal, are subjected to external triangular hydro-sedimentary horizontal loads, inducing convex horizontal deformation. The bottom seal, restrained by pile embedment, experiences buoyant uplift from confined water pressure differentials, resulting in convex vertical deflection [34]. This section employs theoretical analysis to characterize the deformation evolution of steel piles and the bottom seal during cofferdam dewatering construction.

3.1. Idealized Model of Steel Pipe Piles

Based on the staged dewatering excavation and support process, the steel pile deformation evolution is divided into four phases: riverbed excavation, bottom seal construction, dewatering to the second brace level, dewatering to the third brace level, and final dewatering to the seal elevation. Owing to the stabilizing effect of the bottom seal and underlying strata, negligible deformation of the pile base allows the superstructure (above the seal) to be idealized as a single-span or multi-span statically indeterminate cantilever beam system, as illustrated in Figure 3a–d, considering sequential bracing and dewatering operations.

Nodes E, D, C, and B represent the connection points of horizontal braces 1–3 and the bottom seal with the right-side cofferdam steel piles, respectively. The external surface of the steel piles is subjected to hydrostatic and active earth pressures: W_D, W_C, and W_B denote hydrostatic pressures at brace 2, brace 3, and bottom seal elevations, respectively, while S_B is the active earth pressure at the bottom seal. Here, H_w is the vertical distance from the water surface to the bottom seal, and h is the depth from the riverbed to the seal base. Support reactions at nodes E, D, C, B are denoted as F_E, F_D, F_C, F_B, respectively, with corresponding bending moments M_D, M_C, M_B. Clear spans between braces are h_1 (brace 1–2), h_2 (brace 2–3), and h_3 (brace 3–bottom seal). The following are assumed: dewatering steps match brace installation elevations, riverbed elevation is coincident with brace 3 level ($h = h_3$), hydrostatic pressure components are calculated as $W_B = \gamma_w H_w$ and active earth pressure as $S_B = K_a \gamma_s h$, where γ_w is the water unit weight, γ_s is the sand stratum unit weight, and K_a is the active earth pressure coefficient.

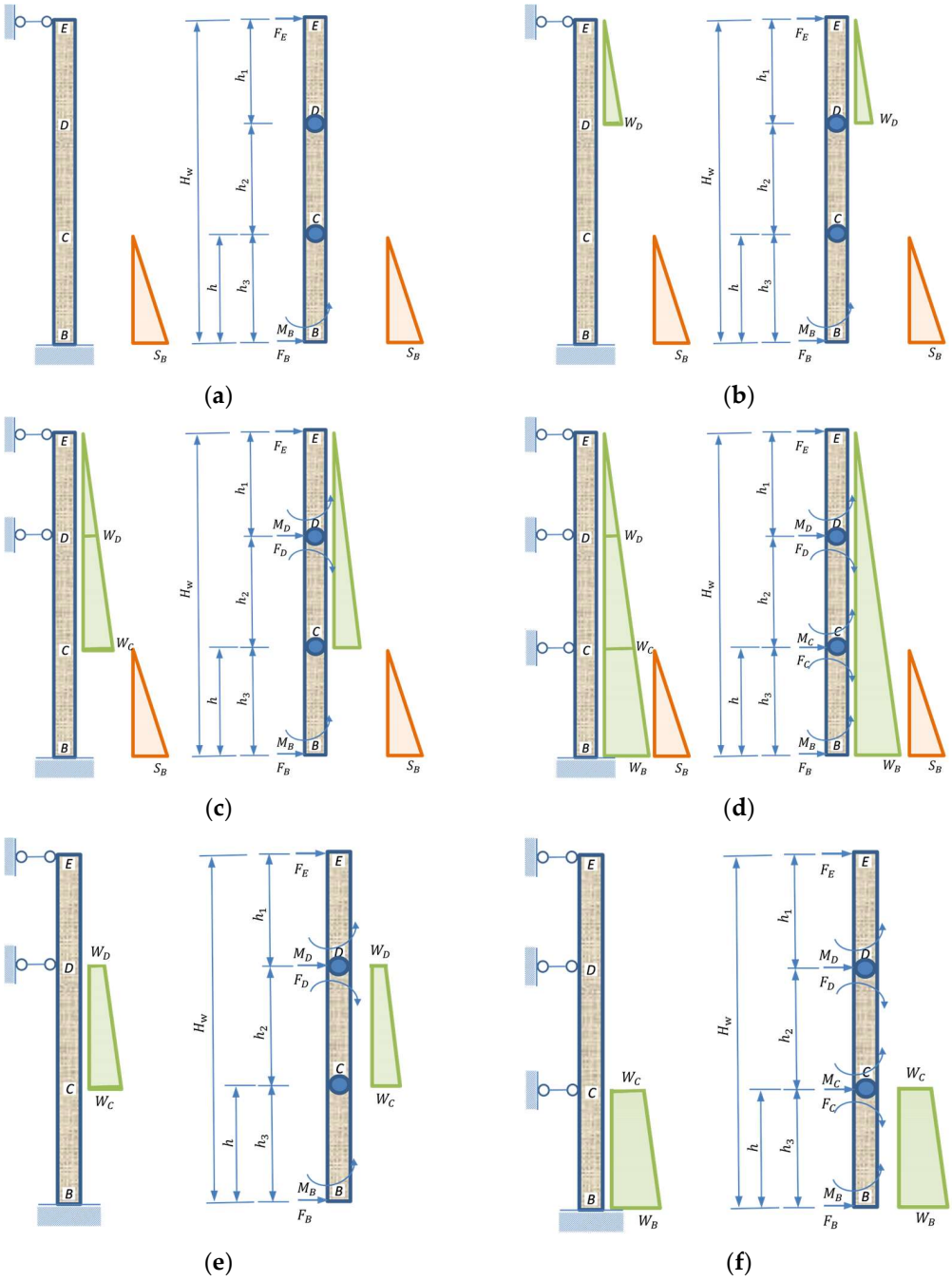

Figure 3. Illustrates the simplified mechanical models for steel pipe piles, including single-span continuous beam models (**a**,**b**), original two/three-span continuous beam models (**c**,**d**), and incremental two/three-span continuous beam models (**e**,**f**).

3.2. Deformation Characteristics of Statically Indeterminate Systems via Simple Beam Superposition

The statically indeterminate cantilever-beam structure is decomposed into a basic statically determinate system (simple supported beam), with rotational angles and deflections derived via load superposition principles. This approach combines the kinematic responses of the simple beam under individual loading conditions to solve for the complex structural behavior [39].

Consider a simple beam AB of length l, with the coordinate origin at A and the x-axis along AB. Point C divides the beam into segments $AC = a$ and $CB = b$ ($a + b = l$), subjected to typical loads including bending moments M, uniform loads q, point loads P,

and trapezoidal pressures. Using the theory of elasticity and beam mechanics, the rotational angle $\theta(x)$ and deflection curve $\omega(x)$ are derived through systematic steps [36]:

Equilibrium Analysis: First, solve the support reactions F_A, F_B via force/moment equilibrium: $\sum F_y = 0$, $\sum M_A = 0$ or $\sum M_B = 0$.

Moment Function Formulation: Establish the bending moment equation $M(x)$ based on load distribution, accounting for discontinuities using singularity functions or piecewise functions.

Differential Equation Integration: Integrate the beam curvature equation $EI\omega''(x) = M(x)$ twice to obtain the following: $EI\theta(x) = \int M(x)dx + C_1$, $EI\omega(x) = \int (\int M(x)dx)dx + C_1x + C_2$. Where C_1, C_2 are integration constants determined by boundary conditions (e.g., $\omega(0) = 0$, $\omega(l) = 0$ for simple supports).

Boundary Condition Application: Enforce geometric compatibility at supports and load application points to solve for C_1, C_2, yielding closed-form solutions for the following: Rotational angles at beam ends: $\theta(A)$, $\theta(B)$. Deflection curves: $\omega(x)$ under each load case.

This method systematically transforms complex indeterminate systems into solvable determinate components, enabling the superposition of individual load effects to characterize the overall deformation behavior of steel pipe piles under staged construction loads.

The expression of the rotational angle $\theta(x)$ and deflection curve $\omega(x)$ of a simply supported beam under typical load conditions are described as follows [39]:

① Simply supported beam AB is subjected to a moment M_A at end A.

$$\omega(x) = \frac{M_A x}{6EIl}\left(2l^2 - 3lx + x^2\right) \tag{1a}$$

$$\theta(x) = \frac{M_A}{6EIl}\left(2l^2 - 6lx + 3x^2\right) \tag{1b}$$

$$\theta(0) = \frac{M_A l}{3EI} \tag{1c}$$

$$\theta(l) = -\frac{M_A l}{6EI} \tag{1d}$$

② Simply supported beam AB is subjected to a moment M_B at end B.

$$\omega(x) = \frac{M_B x}{6EIl}\left(l^2 - x^2\right) \tag{2a}$$

$$\theta(x) = \frac{M_B}{6EIl}\left(l^2 - 3x^2\right) \tag{2b}$$

$$\theta(0) = \frac{M_B l}{6EI} \tag{2c}$$

$$\theta(l) = -\frac{M_B l}{3EI} \tag{2d}$$

③ Simply supported beam AB is subjected to a uniformly distributed load q over the full span.

$$\omega(x) = \frac{qx}{24EI}\left(l^3 - 2lx^2 + x^3\right) \tag{3a}$$

$$\theta(x) = \frac{q}{24EI}\left(l^3 - 6lx^2 + 4x^3\right) \tag{3b}$$

$$\theta(0) = \frac{ql^3}{24EI} \tag{3c}$$

$$\theta(l) = -\frac{ql^3}{24EI} \tag{3d}$$

④ Simply supported beam AB is loaded with a triangular load q over the entire span, where the load intensity increases linearly from zero at end A to q at end B.

$$\omega(x) = \frac{qx}{360EIl}\left(7l^4 - 10l^2x^2 + 3x^4\right) \tag{4a}$$

$$\theta(x) = \frac{q}{360EIl}\left(7l^4 - 30l^2x^2 + 15x^4\right) \tag{4b}$$

$$\theta(0) = \frac{7ql^3}{360EI} \tag{4c}$$

$$\theta(l) = -\frac{ql^3}{45EI} \tag{4d}$$

⑤ Simply supported beam AB is loaded with a triangular load q over the whole span, where the load intensity decreases linearly from q at end A to zero at end B.

$$\omega(x) = \frac{qx}{360EIl}\left(8l^4 - 20l^2x^2 + 15lx^3 - 3x^4\right) \tag{5a}$$

$$\theta(x) = \frac{q}{360EIl}\left(8l^4 - 60l^2x^2 + 60lx^3 - 15x^4\right) \tag{5b}$$

$$\theta(0) = \frac{ql^3}{45EI} \tag{5c}$$

$$\theta(l) = -\frac{7ql^3}{360EI} \tag{5d}$$

⑥ Simply supported beam AB has a uniformly distributed load q over a portion of length a at end A.

$$\omega(x) = \frac{q}{24EIl}\left[lx^4 - 4a\left(l - \frac{a}{2}\right)x^3 + 4a^2\left(l - \frac{a}{2}\right)^2 x\right], \quad (0 \le x \le a) \tag{6a}$$

$$\omega(x) = \frac{qa}{24EIl}\left[-4\left(l - \frac{a}{2}\right)x^3 + 4lx^3 - 6alx^2 + 4a^2lx + 4a\left(l - \frac{a}{2}\right)^2 x - a^3l\right], \quad (a \le x \le l) \tag{6b}$$

$$\theta(x) = \frac{q}{12EIl}\left[2lx^3 - 6a\left(l - \frac{a}{2}\right)x^2 + 2a^2\left(l - \frac{a}{2}\right)^2\right], \quad (0 \le x \le a) \tag{6c}$$

$$\theta(x) = \frac{qa}{12EIl}\left[-6\left(l - \frac{a}{2}\right)x^2 + 6lx^2 - 6alx + 2a^2l + 2a\left(l - \frac{a}{2}\right)^2\right], \quad (a \le x \le l) \tag{6d}$$

$$\theta(0) = \frac{qa^2}{24EIl}(2l - a)^2 \tag{6e}$$

$$\theta(l) = -\frac{qa^2}{24EIl}\left[2l^2 - a^2\right] \tag{6f}$$

⑦ Simply supported beam AB has a uniformly distributed load q over a portion of length b at end B.

$$\omega(x) = -\frac{qb^2}{24EIl}\left(2x^3 - 2l^2x + b^2x\right), \quad (0 \le x \le a) \tag{7a}$$

$$\omega(x) = -\frac{q}{24EIl}\left[2b^2x^3 - 2l^2b^2x + b^4x - l(x - l + b)^4\right], \quad (a \le x \le l) \tag{7b}$$

$$\theta(x) = -\frac{qb^2}{24EIl}\left(6x^2 - 2l^2 + b^2\right), \quad (0 \le x \le a) \tag{7c}$$

$$\theta(x) = -\frac{q}{24EIl}\left[6b^2x^2 - 2l^2b^2 + b^4 - 4l(x - l + b)^3\right], \quad (a \le x \le l) \tag{7d}$$

$$\theta(0) = \frac{qb^2}{24EIl}\left(2l^2 - b^2\right) \tag{7e}$$

$$\theta(l) = -\frac{qb^2}{24EIl}(2l - b)^2 \tag{7f}$$

⑧ Simply supported beam AB has a triangular load q over a portion of length a at end A, with the load intensity decreasing linearly from q at end A to zero at section C.

$$\omega(x) = -\frac{q}{360EIla}\left[3lx^5 - 15alx^4 + 10a^2(3l - a)x^3 + 15a^4lx - 20a^3l^2x - 3a^5x\right], \quad (0 \le x \le a) \tag{8a}$$

$$\omega(x) = -\frac{qa^2}{360EIl}\left(-10x^3 + 30lx^2 - 20l^2x - 3a^2x + 3a^2l\right), \quad (a \le x \le l) \tag{8b}$$

$$\theta(x) = -\frac{q}{360EIla}\left[15lx^4 - 60alx^3 + 30a^2(3l - a)x^2 + 15a^4l - 20a^3l^2 - 3a^5\right], \quad (0 \le x \le a) \tag{8c}$$

$$\theta(x) = -\frac{qa^2}{360EIl}\left(-30x^2 + 60lx - 20l^2 - 3a^2\right), \quad (a \le x \le l) \tag{8d}$$

$$\theta(0) = -\frac{qa^2}{360EIl}\left(15al - 20l^2 - 3a^2\right) \tag{8e}$$

$$\theta(l) = -\frac{qa^2}{360EIl}\left(-3a^2 + 10l^2\right) \tag{8f}$$

⑨ Simply supported beam AB has a triangular load q over a portion of length a at end A, with the load intensity increasing linearly from zero at end A to q at section C.

$$\omega(x) = -\frac{q}{360EIla}\left[-3lx^5 + 10a^2(3l - 2a)x^3 - 40a^3l^2x - 12a^5x + 45a^4lx\right], \quad (0 \le x \le a) \tag{9a}$$

$$\omega(x) = -\frac{qa^2}{360EIl}\left(-20x^3 + 60lx^2 - 40l^2x - 12a^2x + 12a^2l\right), \quad (a \le x \le l) \tag{9b}$$

$$\theta(x) = -\frac{q}{360EIla}\left[-15lx^4 + 30a^2(3l - 2a)x^2 - 40a^3l^2 - 12a^5 + 45a^4l\right], \quad (0 \le x \le a) \tag{9c}$$

$$\theta(x) = -\frac{qa^2}{360EIl}\left(-60x^2 + 120lx - 40l^2 - 12a^2\right), \quad (a \le x \le l) \tag{9d}$$

$$\theta(0) = -\frac{qa^2}{360EIl}\left(45al - 40l^2 - 12a^2\right) \tag{9e}$$

$$\theta(l) = \frac{qa^2}{90EIl}\left(3a^2 - 5l^2\right) \tag{9f}$$

⑩ Simply supported beam AB has a triangular load q over a portion of length b at end B, with the load intensity increasing linearly from zero at section C to q at end B.

$$\omega(x) = -\frac{qb^2}{360EIl}\left(10x^3 - 10l^2x + 3b^2x\right), \quad (0 \le x \le a) \tag{10a}$$

$$\omega(x) = -\frac{q}{360EIlb}\left[10b^3x^3 - 10b^3l^2x + 3b^5x - 3l(x - l + b)^5\right], \quad (a \le x \le l) \tag{10b}$$

$$\theta(x) = -\frac{qb^2}{360EIl}\left(30x^2 - 10l^2 + 3b^2\right), \quad (0 \le x \le a) \tag{10c}$$

$$\theta(x) = -\frac{q}{360EIlb}\left[30b^3x^2 - 15l(x - l + b)^4 - 10b^3l^2 + 3b^5\right], \quad (a \le x \le l) \tag{10d}$$

$$\theta(0) = -\frac{qb^2}{360EIl}\left(3b^2 - 10l^2\right) \tag{10e}$$

$$\theta(l) = \frac{qb^2}{360EIl}\left(15bl - 20l^2 - 3b^2\right) \tag{10f}$$

⑪ Simply supported beam AB has a triangular load q over a portion of length b at end B, with the load intensity decreasing linearly from q at section C to zero at end B.

$$\omega(x) = -\frac{qb^2}{90EIl}\left(5x^3 - 5l^2x + 3b^2x\right), \quad (0 \le x \le a) \tag{11a}$$

$$\omega(x) = -\frac{q}{360EIlb}\left[20b^3x^3 - 15bl(x-l+b)^4 + 3l(x-l+b)^5 - 20b^3l^2x + 12b^5x\right], \quad (a \le x \le l) \tag{11b}$$

$$\theta(x) = -\frac{qb^2}{90EIl}\left(15x^2 - 5l^2 + 3b^2\right), \quad (0 \le x \le a) \tag{11c}$$

$$\theta(x) = -\frac{q}{360EIlb}\left[60b^3x^2 - 60bl(x-l+b)^3 + 15l(x-l+b)^4 - 20b^3l^2 + 12b^5\right], \quad (a \le x \le l) \tag{11d}$$

$$\theta(0) = -\frac{qb^2}{90EIl}\left(3b^2 - 5l^2\right) \tag{11e}$$

$$\theta(l) = \frac{qb^2}{360EIl}\left(45bl - 40l^2 - 12b^2\right) \tag{11f}$$

3.3. Deformation Development Characteristics of Steel Pipe Pile

3.3.1. Stage 1: Riverbed Excavation and Base Sealing Construction

During riverbed excavation for foundation construction, the steel pipe pile is simplified as a single-span cantilever beam model, BE, as shown in Figure 3a. The deflection equation at this stage results from the superposition of triangular loading S_B (Condition ⑧) and bending moment M_B (Condition ①), with a geometric compatibility condition satisfied for the rotation angle at end B, $\theta_{BE} = 0$. For the cantilever beam BE, the following relationships apply:

$$F_E H_w = M_B + \frac{1}{6}S_B {h_3}^2 \tag{12a}$$

$$F_E + F_B = \frac{1}{2}S_B h_3 \tag{12b}$$

$$\frac{M_B H_w}{3EI} - \frac{S_B {h_3}^2}{360EIH_w}\left(15h_3H_w - 20{H_w}^2 - 3{h_3}^2\right) = 0 \tag{12c}$$

Based on the expression group (12), M_B, F_B, and F_E can be obtained:

$$M_B = \frac{S_B {h_3}^2}{120{H_w}^2}\left(15h_3H_w - 20{H_w}^2 - 3{h_3}^2\right) \tag{13a}$$

$$F_E = \frac{S_B {h_3}^2}{120{H_w}^3}\left(15h_3H_w - 20{H_w}^2 - 3{h_3}^2\right) + \frac{1}{6H_w}S_B {h_3}^2 \tag{13b}$$

$$F_B = \frac{1}{2}S_B h_3 - \frac{S_B {h_3}^2}{120{H_w}^3}\left(15h_3H_w - 20{H_w}^2 - 3{h_3}^2\right) - \frac{1}{6H_w}S_B {h_3}^2 \tag{13c}$$

By combining the above equations and taking support B as the coordinate origin (with the x-axis along the beam axis), the deflection deformation expression of the steel pipe pile at this construction stage is derived by superimposing the solutions for simply supported beam conditions ① and ⑧:

$$\begin{aligned}\omega(x) = &-\frac{S_B}{360EIH_wh_3}\left[3H_wx^5 - 15h_3H_wx^4 + 10{h_3}^2(3H_w - h_3)x^3 + 15{h_3}^4H_wx - 20{h_3}^3{H_w}^2x - 3{h_3}^5x\right] \\ &+\frac{M_Bx}{6EIH_w}\left(2{H_w}^2 - 3H_wx + x^2\right), \quad (0 \le x \le h_3)\end{aligned} \tag{14a}$$

$$\begin{aligned}\omega(x) = &-\frac{S_B{h_3}^2}{360EIH_w}\left(-10x^3 + 30H_wx^2 - 20{H_w}^2x - 3{h_3}^2x + 3{h_3}^2H_w\right) + \frac{M_Bx}{6EIH_w}\left(2{H_w}^2 - 3H_wx + x^2\right), \\ &(h_3 \le x \le H_w)\end{aligned} \tag{14b}$$

3.3.2. Stage 2: Installation of the Second Support

During the installation of the second support, the steel pipe pile is simplified as a single-span cantilever beam model, BE, as illustrated in Figure 3b. The deflection equation at this stage results from the superposition of triangular loads S_B and W_D defined in conditions ⑧ and conditions ⑪, combined with the moment load M_B in Case ①. The geometric compatibility condition, $\theta_{BE} = 0$, for the rotation angle at end B is satisfied. For the cantilever beam BE, the following relationships hold:

$$F_E + F_B = \frac{1}{2}S_B h_3 + \frac{1}{2}W_D h_1 \tag{15a}$$

$$F_E H_w = M_B + \frac{1}{2}W_D h_1\left(H_w - \frac{2}{3}h_1\right) + \frac{1}{6}S_B {h_3}^2 \tag{15b}$$

$$\frac{M_B H_w}{3EI} + \frac{S_B {h_3}^2}{360EIH_w}\left(15h_3 H_w - 20{H_w}^2 - 3{h_3}^2\right) - \frac{W_D {h_1}^2}{90EIH_w}\left(3{h_1}^2 - 5{H_w}^2\right) = 0 \tag{15c}$$

Based on the expression group (15), M_B, F_B and F_E can be obtained:

$$M_B = -\frac{S_B {h_3}^2}{120{H_w}^2}\left(15h_3 H_w - 20{H_w}^2 - 3{h_3}^2\right) + \frac{W_D {h_1}^2}{30{H_w}^2}\left(3{h_1}^2 - 5{H_w}^2\right) \tag{16a}$$

$$F_E = -\frac{S_B {h_3}^2}{120{H_w}^3}\left(15h_3 H_w - 20{H_w}^2 - 3{h_3}^2\right) + \frac{W_D {h_1}^2}{30{H_w}^3}\left(3{h_1}^2 - 5{H_w}^2\right) + \frac{1}{2}\frac{W_D}{H_w}h_1\left(H_w - \frac{2}{3}h_1\right) + \frac{1}{6H_w}S_B {h_3}^2 \tag{16b}$$

$$F_B = \tfrac{1}{2}S_B h_3 + \tfrac{1}{2}W_D h_1 + \tfrac{S_B {h_3}^2}{120{H_w}^3}\left(15h_3 H_w - 20{H_w}^2 - 3{h_3}^2\right) - \tfrac{W_D {h_1}^2}{30{H_w}^3}\left(3{h_1}^2 - 5{H_w}^2\right) - \tfrac{1}{2}\tfrac{W_D}{H_w}h_1\left(H_w - \tfrac{2}{3}h_1\right) - \tfrac{1}{6H_w}S_B {h_3}^2 \tag{16c}$$

By solving the above equations and establishing a coordinate system with support B as the origin (x-axis along the beam axis), the deflection deformation expression of the steel pipe pile at this construction stage is derived through the superposition of simply supported beam conditions ①, ⑧, and ⑪:

$$\omega(x) = -\tfrac{S_B}{360EIH_w h_3}\left[3H_w x^5 - 15h_3 H_w x^4 + 10{h_3}^2(3H_w - h_3)x^3 + 15{h_3}^4 H_w x - 20{h_3}^3{H_w}^2 x - 3{h_3}^5 x\right] + \tfrac{M_B x}{6EIH_w}\left(2{H_w}^2 - 3H_w x + x^2\right) - \tfrac{W_D {h_1}^2}{90EIH_w}\left(5x^3 - 5{H_w}^2 x + 3{h_1}^2 x\right),\ (0 \le x \le h_3) \tag{17a}$$

$$\omega(x) = -\tfrac{S_B {h_3}^2}{360EIH_w}\left(-10x^3 + 30H_w x^2 - 20{H_w}^2 x - 3{h_3}^2 x + 3{h_3}^2 H_w\right) + \tfrac{M_B x}{6EIH_w}\left(2{H_w}^2 - 3H_w x + x^2\right) - \tfrac{W_D {h_1}^2}{90EIH_w}\left(5x^3 - 5{H_w}^2 x + 3{h_1}^2 x\right),\ (h_3 \le x \le h_3 + h_2) \tag{17b}$$

$$\omega(x) = -\tfrac{S_B {h_3}^2}{360EIH_w}\left(-10x^3 + 30H_w x^2 - 20{H_w}^2 x - 3{h_3}^2 x + 3{h_3}^2 H_w\right) + \tfrac{M_B x}{6EIH_w}\left(2{H_w}^2 - 3H_w x + x^2\right) - \tfrac{W_D}{360EIH_w h_1}\left[20{h_1}^3 x^3 - 15h_1 H_w(x - H_w + h_1)^4 + 3H_w(x - H_w + h_1)^5 - 20{h_1}^3{H_w}^2 x + 12{h_1}^5 x\right],\ (h_3 + h_2 \le x \le H_w) \tag{17c}$$

3.3.3. Stage 3: Installation of the Third Support

During the installation of the third support (Figure 3c), the steel pipe pile is simplified as a two-span cantilever continuous beam model, BE. While the deflection expression could theoretically be derived by superimposing simply supported beam conditions ⑧, ①, ⑦–⑪, ②, and ⑤, ①, direct superposition of the current deflection curve would disregard deformations from the first two stages, leading to result distortion, due to the construction of the new horizontal support D. Thus, the horizontal deformation of the steel pipe pile at this stage is approximated using an incremental method.

The displacement increment in Stage 3 is attributed to the trapezoidal load W_D&W_C acting on the two-span cantilever continuous beam BE shown in Figure 3e. The deflection

equation combines the segment BC bending moment M_B (Condition ①), segment CD trapezoidal load W_D & W_C (Conditions ⑦ and ⑪), end D bending moment M_D (Condition ②), segment DE bending moment M_D (Condition ①), and geometric compatibility conditions: equal rotation angle at end B, $\theta_{BD} = 0$ and equal rotation angles on both sides of support D, $\theta_{DE} = \theta_{DC}$. For the cantilever continuous beam BE, the following relationships hold:

$$F_E h_1 = M_D \tag{18a}$$

$$F_D(h_2+h_3) = M_B - M_D + W_D h_2\left(\frac{1}{2}h_2 + h_3\right) + \frac{1}{2}(W_C - W_D)h_2\left(\frac{1}{3}h_2 + h_3\right) \tag{18b}$$

$$F_E + F_D + F_B = \frac{1}{2}(W_C + W_D)h_2 \tag{18c}$$

$$\begin{aligned}&\tfrac{M_B(h_2+h_3)}{3EI} + \tfrac{M_D(h_2+h_3)}{6EI} + \tfrac{W_D {h_2}^2}{24EI(h_2+h_3)}\left({h_2}^2 + 2{h_3}^2 + 4h_2h_3\right)\\ &\quad + \tfrac{(W_C-W_D){h_2}^2}{90EI(h_2+h_3)}\left(2{h_2}^2 + 5{h_3}^2 + 10h_2h_3\right) = 0\end{aligned} \tag{18d}$$

$$\begin{aligned}&-\tfrac{M_B(h_2+h_3)}{6EI} - \tfrac{M_D(h_2+h_3)}{3EI} - \tfrac{W_D {h_2}^2}{24EI(h_2+h_3)}(h_2+2h_3)^2\\ &\quad - \tfrac{(W_C-W_D){h_2}^2}{360EI(h_2+h_3)}\left(40{h_3}^2 + 35h_2h_3 + 7{h_2}^2\right) = \tfrac{M_D h_1}{3EI}\end{aligned} \tag{18e}$$

Based on the expression group (18), M_B, M_D, F_B, F_D, and F_E can be obtained:

$$M_D = \frac{1}{4h_1+3h_2+3h_3}\left[W_D\frac{{h_2}^2\left(-{h_2}^2-6{h_3}^2-4h_2h_3\right)}{4(h_2+h_3)} - (W_C-W_D)\frac{{h_2}^2\left(10{h_3}^2+5h_2h_3+{h_2}^2\right)}{10(h_2+h_3)}\right] \tag{19a}$$

$$F_E = \frac{1}{h_1(4h_1+3h_2+3h_3)}\left[W_D\frac{{h_2}^2\left(-{h_2}^2-6{h_3}^2-4h_2h_3\right)}{4(h_2+h_3)} - (W_C-W_D)\frac{{h_2}^2\left(10{h_3}^2+5h_2h_3+{h_2}^2\right)}{10(h_2+h_3)}\right] \tag{19b}$$

$$\begin{aligned}M_B = &-\tfrac{1}{2(4h_1+3h_2+3h_3)}\left[W_D\tfrac{{h_2}^2\left(-{h_2}^2-6{h_3}^2-4h_2h_3\right)}{4(h_2+h_3)} - (W_C-W_D)\tfrac{{h_2}^2\left(10{h_3}^2+5h_2h_3+{h_2}^2\right)}{10(h_2+h_3)}\right]\\ &-\tfrac{W_D{h_2}^2}{8(h_2+h_3)^2}\left({h_2}^2+2{h_3}^2+4h_2h_3\right) - \tfrac{(W_C-W_D){h_2}^2}{30(h_2+h_3)^2}\left(2{h_2}^2+5{h_3}^2+10h_2h_3\right)\end{aligned} \tag{19c}$$

$$\begin{aligned}F_D = &-\tfrac{3}{2(4h_1+3h_2+3h_3)(h_2+h_3)}\left[W_D\tfrac{{h_2}^2\left(-{h_2}^2-6{h_3}^2-4h_2h_3\right)}{4(h_2+h_3)} - (W_C-W_D)\tfrac{{h_2}^2\left(10{h_3}^2+5h_2h_3+{h_2}^2\right)}{10(h_2+h_3)}\right]\\ &+W_D\tfrac{h_2\left(\frac{1}{2}h_2+h_3\right)}{(h_2+h_3)} - W_D\tfrac{{h_2}^2\left({h_2}^2+2{h_3}^2+4h_2h_3\right)}{8(h_2+h_3)^3} - (W_C-W_D)\tfrac{{h_2}^2\left(2{h_2}^2+5{h_3}^2+10h_2h_3\right)}{30(h_2+h_3)^3}\\ &+(W_C-W_D)\tfrac{h_2\left(\frac{1}{3}h_2+h_3\right)}{2(h_2+h_3)}\end{aligned} \tag{19d}$$

$$\begin{aligned}F_B = &\tfrac{1}{(4h_1+3h_2+3h_3)}\left[\tfrac{3}{2(h_2+h_3)} - \tfrac{1}{h_1}\right]\left[W_D\tfrac{{h_2}^2\left(-{h_2}^2-6{h_3}^2-4h_2h_3\right)}{4(h_2+h_3)} - (W_C-W_D)\tfrac{{h_2}^2\left(10{h_3}^2+5h_2h_3+{h_2}^2\right)}{10(h_2+h_3)}\right]\\ &+W_D\tfrac{{h_2}^2\left({h_2}^2+2{h_3}^2+4h_2h_3\right)}{8(h_2+h_3)^3} - W_D\tfrac{h_2\left(\frac{1}{2}h_2+h_3\right)}{(h_2+h_3)} + \tfrac{1}{2}(W_C+W_D)h_2\\ &+(W_C-W_D)\tfrac{{h_2}^2\left(2{h_2}^2+5{h_3}^2+10h_2h_3\right)}{30(h_2+h_3)^3} - (W_C-W_D)\tfrac{h_2\left(\frac{1}{3}h_2+h_3\right)}{2(h_2+h_3)}\end{aligned} \tag{19e}$$

By solving the above equations and establishing a coordinate system with support B as the origin (x-axis along the beam axis), the incremental deflection expression of the steel pipe pile is derived through the superposition of simply supported beam conditions ①, ⑦–⑪, ②, and ①.

$$\begin{aligned}\omega(x) = &\tfrac{M_B x}{6EI(h_2+h_3)}\left(2(h_2+h_3)^2 - 3(h_2+h_3)x + x^2\right) + \tfrac{M_D x}{6EI(h_2+h_3)}\left((h_2+h_3)^2 - x^2\right)\\ &-\tfrac{W_D{h_2}^2}{24EI(h_2+h_3)}\left(2x^3 - 2(h_2+h_3)^2x + {h_2}^2x\right) - \tfrac{(W_C-W_D){h_2}^2}{90EI(h_2+h_3)}\left(5x^3 - 5(h_2+h_3)^2x + 3{h_2}^2x\right),\\ &(0 \le x \le h_3)\end{aligned} \tag{20a}$$

$$\begin{aligned}\omega(x) = {} & \frac{M_B x}{6EI(h_2+h_3)}\left(2(h_2+h_3)^2 - 3(h_2+h_3)x + x^2\right) + \frac{M_D x}{6EI(h_2+h_3)}\left((h_2+h_3)^2 - x^2\right) \\ & - \frac{W_D}{24EI(h_2+h_3)}\left[2{h_2}^2x^3 - 2(h_2+h_3)^2{h_2}^2x + {h_2}^4x - (h_2+h_3)(x-h_3)^4\right] \\ & - \frac{(W_C-W_D)}{360EI(h_2+h_3)h_2}\left[20{h_2}^3x^3 - 15h_2(h_2+h_3)(x-h_3)^4 + 3(h_2+h_3)(x-h_3)^5 - 20{h_2}^3(h_2+h_3)^2x + 12{h_2}^5x\right], \\ & (h_3 \le x \le h_3+h_2)\end{aligned} \tag{20b}$$

$$\omega(x) = \frac{M_D(x-h_3-h_2)}{6EIh_1}\left[2{h_1}^2 - 3h_1(x-h_3-h_2) + (x-h_3-h_2)^2\right], \quad (h_3+h_2 \le x \le H_w) \tag{20c}$$

3.3.4. Stage 4: Precipitation Completion

During the precipitation completion stage, the steel pipe pile is simplified as a three-span cantilever continuous beam model (Figure 3d). Direct superposition of statically determinate system deflections would similarly distort results, so an incremental method analogous to Stage 3 is adopted.

The fourth-stage displacement increment is approximated by the trapezoidal load W_C&W_B acting on the two-span cantilever continuous beam, BE, in Figure 3f. The deflection equation incorporates segment BC bending moment M_B (Condition ①), trapezoidal load W_C & W_B (Conditions ③–⑤), end C bending moment M_C (Condition ②), segment CD bending moment M_D (Condition ②) and ending moment M_C (Condition ①), segment DE bending moment M_D (Condition ①), and geometric compatibility conditions: equal rotation angles at end B, $\theta_{BD} = 0$, support D, $\theta_{DE} = \theta_{DC}$, and support C, $\theta_{CD} = \theta_{CB}$. For the cantilever continuous beam BE, the following relationships are satisfied:

$$F_E h_1 = M_D \tag{21a}$$

$$F_D h_2 = M_C - M_D \tag{21b}$$

$$F_C h_3 = M_B - M_C + \frac{1}{2}W_C{h_3}^2 + \frac{1}{6}(W_B - W_C){h_3}^2 \tag{21c}$$

$$F_E + F_D + F_C + F_B = \frac{1}{2}(W_B + W_C)h_3 \tag{21d}$$

$$\frac{M_B h_3}{3EI} + \frac{M_C h_3}{6EI} + \frac{W_C{h_3}^3}{24EI} + \frac{(W_B - W_C){h_3}^3}{45EI} = 0 \tag{21e}$$

$$-\frac{M_B h_3}{6EI} - \frac{M_C h_3}{3EI} - \frac{W_C{h_3}^3}{24EI} - \frac{7(W_B - W_C){h_3}^3}{360EI} = \frac{M_C h_2}{3EI} + \frac{M_D h_2}{6EI} \tag{21f}$$

$$-\frac{M_C h_2}{6EI} - \frac{M_D h_2}{3EI} = \frac{M_D h_1}{3EI} \tag{21g}$$

Based on the expression group (21), M_B, M_C, M_D, F_B, F_C, F_D, and F_E can be obtained:

$$M_C = -\frac{(h_1+h_2){h_3}^3}{20(4h_2+3h_3)(h_1+h_2) - 20{h_2}^2}[2(W_B - W_C) + 5W_C] \tag{22a}$$

$$M_B = -\frac{1}{2}M_C - \frac{W_C{h_3}^2}{8} - \frac{(W_B - W_C){h_3}^2}{15} \tag{22b}$$

$$M_D = -\frac{h_2}{2(h_1+h_2)}M_C \tag{22c}$$

$$F_E = -\frac{h_2}{2h_1(h_1+h_2)}M_C \tag{22d}$$

$$F_D = \frac{1}{h_2}\left(1 + \frac{h_2}{2(h_1+h_2)}\right)M_C \tag{22e}$$

$$F_C = -\frac{3}{2h_3}M_C + \frac{3}{8}W_C h_3 + \frac{1}{10}(W_B - W_C)h_3 \tag{22f}$$

$$F_B = \left[\frac{h_2}{2h_1(h_1+h_2)} - \frac{1}{h_2} - \frac{1}{2(h_1+h_2)} + \frac{3}{2h_3}\right]M_C - \frac{3}{8}W_C h_3 - \frac{1}{10}(W_B - W_C)h_3 + \frac{1}{2}(W_B + W_C)h_3 \quad (22g)$$

By solving the above equations and maintaining the coordinate system with support B as the origin, the incremental deflection expression is obtained via superposition of conditions ①, ③–⑤, ② and ②, ① as well as ①.

$$\begin{aligned}\omega(x) = {} & \frac{M_B x}{6EIh_3}\left(2{h_3}^2 - 3h_3 x + x^2\right) + \frac{M_C x}{6EIh_3}\left({h_3}^2 - x^2\right) + \frac{W_C x}{24EI}\left({h_3}^3 - 2h_3 x^2 + x^3\right) \\ & + \frac{(W_B - W_C)x}{360EIh_3}\left(8{h_3}^4 - 20{h_3}^2 x^2 + 15h_3 x^3 - 3x^4\right), \quad (0 \le x \le h_3)\end{aligned} \quad (23a)$$

$$\omega(x) = \frac{M_C(x-h_3)}{6EIh_2}\left[2{h_2}^2 - 3h_2(x-h_3) + (x-h_3)^2\right] + \frac{M_D(x-h_3)}{6EIh_2}\left[{h_2}^2 - (x-h_3)^2\right], \quad (h_3 \le x \le h_3 + h_2) \quad (23b)$$

$$\omega(x) = \frac{M_D(x-h_3-h_2)}{6EIh_1}\left[2{h_1}^2 - 3h_1(x-h_3-h_2) + (x-h_3-h_2)^2\right], \quad (h_3 + h_2 \le x \le H_w) \quad (23c)$$

This incremental deflection (Equation (23)) is superimposed onto the Stage 2 (Equation (17)) and Stage 3 (Equation (20)) deflections to derive the total deformation. A full-load analysis based on Figure 3d is necessary to calculate the additional bending moment and horizontal load at end B.

3.4. Deformation Characteristics of the Bottom Sealing

To analyze the stress-deformation behavior of the concrete bottom sealing, the material is idealized as a continuous, uniform, isotropic medium undergoing small deformations [36]. A unit-width lining segment is selected for stress analysis, which can be simplified as a beam AB with length l and thickness t, as depicted in Figure 4.

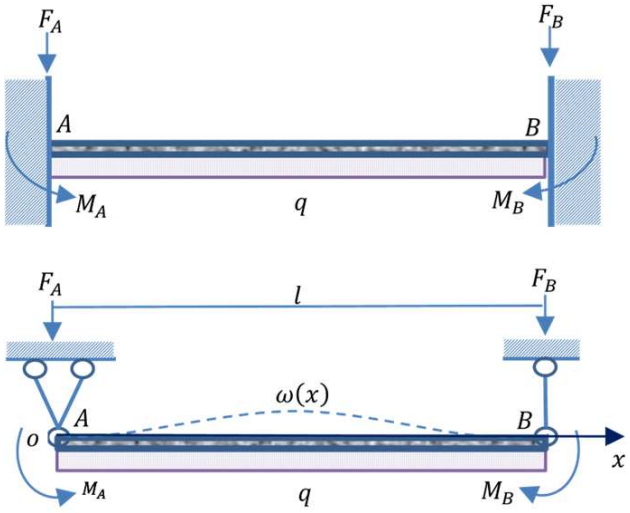

Figure 4. Calculation model for cofferdam bottom sealing.

The base structure is primarily subjected to three vertical actions: self-weight $G = \gamma tl$, adhesive force $f_1 = \sigma l$ between the base and underlying stratum, and water buoyancy $f_2 = \gamma_w h_w l$. Here, γ denotes the specific weight of base concrete, σ the adhesive strength per unit area between the base and stratum, γ_w the specific weight of water, and h_w the difference in water levels inside and outside the cofferdam. The base is thus modeled as a doubly fixed-end beam AB under an equivalent uniform distributed load $q = \gamma_w h_w - \gamma t - \sigma$. According to the theory of material mechanics, the vertical load $F_A = F_B = \frac{ql}{2}$ and end bending moments $M_A = M_B$ of this statically indeterminate beam

are analyzed by selecting a simply supported beam as the basic static system. The geometric compatibility equation for the rotational deformation at support A is expressed as follows:

$$\theta_A = \theta_{Aq} + \theta_{AM_A} + \theta_{AM_B} = 0 \tag{24}$$

where, θ_A is the total rotation angle at support A, θ_{Aq}, θ_{AM_A}, and θ_{AM_B} denote the rotational angles at A induced by the uniform load q, support bending moment M_A, and support B bending moment M_B, respectively.

Substituting the force–rotation angle relationships Equations (1)–(3) for ①②③ working conditions into Equation (24), the fixed-end bending moments $M_A = -\frac{ql^2}{12}$ is derived. Taking support A as the coordinate origin and the beam axis as the x-axis, the bending moment at any position x along the fixed-end beam is as follows:

$$M(x) = -\frac{qx^2}{2} + \frac{qlx}{2} - \frac{ql^2}{12} \tag{25}$$

Using the differential relationship between bending moment and deflection curve ($EI\omega''(x) = -M(x)$) and applying the fixed-end boundary conditions ($x = 0$, $\omega(x) = 0$, $x = l$, $\omega(x) = 0$), the deflection curve equation is obtained as follows:

$$\omega(x) = \frac{1}{EI}\left(-\frac{qx^4}{24} + \frac{qlx^3}{12} - \frac{ql^2x^2}{24}\right) \tag{26}$$

The maximum midspan deflection under vertical loading is $\omega_0 = \frac{ql^4}{384EI}$. For the vertical deformation of the bottom sealing, in addition to the effective vertical load q, the additional bending moment M_{0B} and horizontal load F_{0B} at support B, resulting from the differential water and soil pressure at the ends of the steel pipe piles must be considered. As the foundation pit water level is gradually lowered, these additional loads increase incrementally. Thus, only the deformations induced during the fourth-stage precipitation to the casting stage are analyzed. The midspan deflection due to the end additional bending moment M_{0B} at casting completion is $\Delta_{M_0} = \frac{M_{0B}l^2}{16EI}$, and the shrinkage deformation from the end additional forces F_{0B} is $\Delta_{F_{0B}} = \frac{F_{0B}l}{EA}$. Using the triangular relationship for deformed pressure-bending members, the vertical midspan deformation $\Delta_{F_0} = \sqrt{\frac{l\Delta_{F_{0B}}}{2} - \frac{{\Delta_{F_{0B}}}^2}{4}}$ caused by horizontal compression of the bottom sealing is derived. The total midspan deformation during casting is therefore the superposition of these components:

$$\Delta l = \omega_0 - 2\Delta_{M_0} + \Delta_{F_0} \tag{27}$$

4. Verification and Application

The theoretical framework developed in the preceding section is validated and applied to the steel pipe pile cofferdam foundation pit engineering of the 6# pier of the Jingwei River-Rail Shared Bridge of Xi'an Metro Line 10 (China), as shown in Figure 5a. The primary sub-riverbed soil layer at this site is medium sand, characterized by specific physical-mechanical properties and permeability, as shown in Figure 5b. As illustrated in Figure 5c, the 6# pier employs a Φ 820 × 16 mm interlocking steel pipe pile cofferdam with a 33 m pile length, 1 m spacing, and CT-type pile interlocks. The internal supports consist mainly of HN 900 × 300 and HM 550 × 300 H-shaped steel sections and Φ 630 × 10 steel pipes.

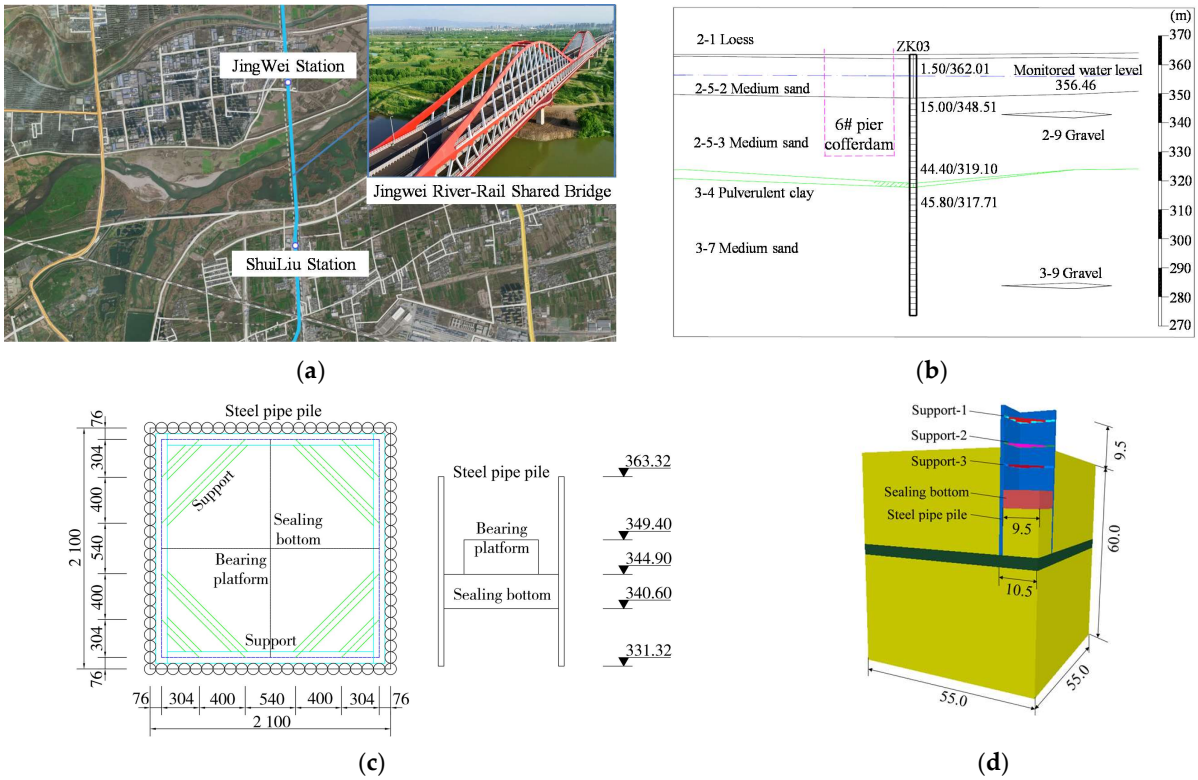

Figure 5. (**a**) Outdoor scene, (**b**) stratum distribution, (**c**) structural design, and (**d**) numerical model of 6# pier steel pipe pile cofferdam.

Construction process of the cofferdam foundation pit:

a. Underwater base cleaning to elevation 354.80 m.
b. Install first and second steel pipe pile rings underwater, using the first ring as a guide for driving interlocking steel pipe piles.
c. Excavate the pit interior from elevation 354.80 m to 340.60 m and construct underwater bottom sealing concrete.
d. Drain water to 1 m below the first ring (360.82 m) and install the first-level internal support at 361.82 m.
e. Drain to 1 m below the second ring (354.82 m) and install the second-level internal support at 355.82 m.
f. Drain to 1 m below the third ring (349.82 m), install the third ring and corresponding internal support at 350.82 m.
g. Drain remaining water to 344.90 m, construct the cap, then remove the third ring and support, followed by main pier construction.
h. After pier completion, refill the cofferdam to 1 m below the second ring and remove the second ring and support. Continue refilling to the river surface level and dismantle the first ring and support.

Field measurements for the cofferdam foundation pit engineering project primarily involve monitoring the horizontal displacement of the steel pipe pile top using a total station with an accuracy of 0.5″ and 0.8 mm + 1 ppm, the vertical displacement via a leveling instrument with a precision of 0.3 mm/km, the deep horizontal displacement through an inclinometer with a sensitivity of ±0.01 mm per 500 mm measurement interval, and the pit edge surface subsidence by the same leveling instrument, complemented by internal support axial force and groundwater level monitoring. Displacement observation points are strategically positioned at the midpoints of the cofferdam's four sides, while vertical observation points for deep horizontal deformation analysis of steel pipe piles are spaced

at 1.0 m intervals, with all measurement procedures and methodologies strictly adhering to the protocols specified in relevant industry standards and technical specifications.

4.1. Model Establishment

A 1/4 symmetry model is developed for the 21.0 m × 21.0 m × 14.2 m cofferdam foundation pit (Figure 5d) to optimize computational efficiency. Deep horizontal deformation monitoring points are distributed at 1.0 m intervals along the pile body at the midpoint of each cofferdam side in order to be consistent with the actual field monitoring points' position.

The model boundaries enforce normal displacement constraints on vertical sides and full displacement constraints on the base, with the above boundaries set as impermeable. The steel pipe pile adopts the impermeable null model, and the weak permeable sealing layer is set according to the coefficient of permeability of concrete. Water surfaces are considered to simulate the hydraulic boundary conditions, including a constant external design water level and internal changeable water levels corresponding to the 1st–4th dewatering stages and 1st–2nd refilling stages per the construction sequence. The initial conditions mainly include the stress field under the condition of stratum self-weight, the structural stress field under the recommended lateral pressure coefficient, the pore pressure field under the design water level and hydrostatic pressure, etc.

The stratum and steel pipe piles are simulated using solid elements, while supports are modeled as beam elements. The steel pipe piles adopt a linear elastic constitutive model, the stratum uses a Mohr-Coulomb (M-C) model, and seepage is governed by an isotropic permeability model.

4.2. Parameter Selection

The relevant survey data provided by the survey and design departments for the cofferdam foundation pit project shows that the primary soil stratum at this site is medium sand, and the sequence under the water surface is 2-5-2 medium sand with an average thickness of 7.95 m, 2-5-3 medium sand with an average thickness of 29.40 m, and a uneven thickness and distribution of 3–4 silty clay intercalation, as showed in Figure 5b. Mainly conducted particle analysis tests on disturbed sand samples, shear tests on undisturbed samples, and also conducted standard penetration tests, static cone penetration tests, wave velocity tests, resistivity tests, etc., on site. In combination with relevant specifications, manuals, regional experience, and site conditions, the physical and index suggested value of the site stratum rock and soil was determined comprehensively.

The design water level of this cofferdam is 363.32 m, the pile top elevation is 364.32 m, the pile length is 33 m, and the elevation of the riverbed after cleaning is 354.80 m, that, the depth of the steel pipe pile embedded into the stratum is 23.48 m, and they are all in the medium sand layer with good permeability. Our team has conducted a large number of numerical analyses on the sensitivity of stratum parameters in the early stage [37,38], as the parameters of the two sandy layers are very close the impact on the deformation of the cofferdam support structure is very small, so in this calculation analysis, it can be simplified and considered according to its average value. Based on the investigation and design data of the cofferdam foundation pit, the basic physical and mechanical parameters of each stratum are listed in Table 1. And the unit weight of the steel pipe pile, support, and internal support structure is 78.5 kN/m^3, with an elastic modulus of 206 GPa and a Poisson's ratio of 0.25.

Table 1. Physical and mechanical parameters of strata.

Lamination Characteristics	2-5-2 Medium Sand	2-5-3 Medium Sand	Average Medium Sand
Natural bulk density, γ/(kN·m^{-3})	19.5	20.5	20.0
Saturated bulk density, γ_{sat}/(kN·m^{-3})	22.8	23.8	23.3
Compressive modulus, E_s/MPa	25.0	27.0	26.0
Deformation modulus, E/MPa	40.0	46.0	43.0
Cohesion, c/kPa	2.0	2.0	2.0
Angle of internal friction, φ/(°)	36.0	38.0	37.0
Poisson's ratio, μ		0.27	
Side pressure coefficient, λ		0.37	
Porosity, n		0.33	
Saturation, S_r		1.0	
Permeability coefficient, K/(cm·s^{-1})		10^{-5}	

4.3. Deformation of Steel Pipe Pile

Considering the geological conditions and construction technology of the cofferdam project, a hydrological–mechanical coupling simulation was conducted for the entire construction process to analyze the evolutionary characteristics of steel pipe pile deformation during dewatering. The analysis of the cofferdam foundation pit dewatering excavation, the initial stress field, and pore pressure field are theoretically checked first, and the subsequent calculation analysis is based on the initial field check of the model, which can ensure the accuracy of the subsequent calculation analysis.

The horizontal deformation at different depths under each working condition exhibits a consistent convex profile along the depth direction, with an overall trend of increasing first and then decreasing as the construction progresses, as illustrated in Figure 6. Upon completion of the main pier construction, the maximum deformation of 20.72 mm occurs at a depth of 14 m below the pile top. The field-measured horizontal deformation reflecting the deep horizontal displacement of the soil outside the pile aligns well with the simulation and theoretical results in terms of deformation pattern, despite slight discrepancies in magnitude. This consistency is attributed to factors such as the actual external water level being lower than the design value during monitoring and the field construction progress entering the water refilling stage.

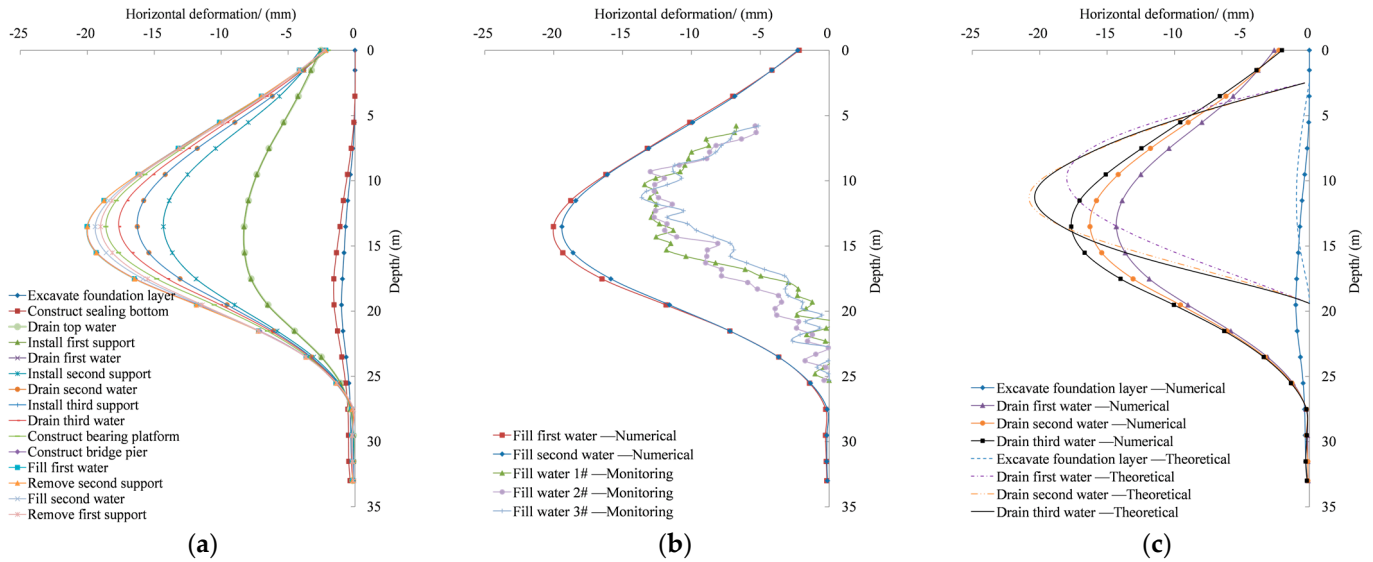

Figure 6. Horizontal deformation of steel pipe piles: (**a**) numerical simulation, (**b**) field measurement, and (**c**) theoretical prediction.

4.4. Bottom Sealing Deformation

The bottom sealing of this cofferdam foundation pit is constructed with C30 concrete (thickness $t_1 = 4.3$ m, length $l = 21$ m) and supported by internal braces with a spacing of $h_1 = 6.0$ m, $h_2 = 5.0$ m, $h_3 = 5.9$ m. The active earth pressure coefficient outside the steel pipe pile is $K_a = 0.25$, and the active earth pressure at support B is $S_B = 27.83$ kPa. The static water pressures outside the pile are $W_D = 60.0$ kPa, $W_C = 110.0$ kPa, $W_B = 169.0$ kPa at different elevations.

Additional loads on support B induced by differential water and soil pressures are denoted as $F_{0B} = 839.13$ kN and $M_{0B} = 1\,102.38$ kN·m. Under the equivalent uniformly distributed load $q = 62.50$ kN/m, the midspan deformation of the concrete bottom sealing due to vertical loading is $\omega_0 = 0.15$ mm. The midspan deflections caused by the additional bending moment and horizontal load are 0.29 mm and 36.96 mm, respectively. The total midspan deformation of the bottom sealing, $\Delta l = 37.40$ mm, agrees well with the numerical analysis result of 40.10 mm for the relative deformation between the midspan and ends of the bottom sealing. Meanwhile, the total midspan deformation of the bottom sealing is measured as 11.26 mm, 14.39 mm, and 21.93 mm during Stage 1, Stage 2, and Stage 3, respectively.

5. Discussion

The steel pipe and the bottom seal in the cofferdam structure interact and are embedded in the stratum. The difference in hydrostatic pressure inside and outside the cofferdam can cause horizontal deformation of the pile body and uplift deformation of the bottom seal concrete. When the deformation is excessive, it can lead to cracks between piles and concrete cracks, and then lead to risks such as seepage and even piping failure, which are the main risks of the steel pipe pile cofferdam [1]. In addition, there are also potential risks of damage to the cofferdam structure caused by normal flow, flood, and surging, and potential risks under impact and scouring [27–30]. At the same time, the quality of underwater bottom seal concrete is difficult to guarantee, so it is impossible to guarantee that the thickness is consistent in all parts or that there is no defect in the interior.

The steel pipe pile cofferdam is equivalent to a fixed-end multi-span continuous wall according to the bending characteristics, and the optimization of the section size or that of the steel pipe pile can be considered, which can optimize the amount of steel used while ensuring the deformation stability and safety of the steel pipe pile, thereby reducing investment [15,19,20]. The concrete bottom seal is equivalent to a fixed-end beam, and the thickness and grade of the bottom seal concrete can be considered, which can optimize the amount of concrete used while ensuring the deformation stability and safety of the bottom seal, thereby reducing investment.

In the stress-deformation analysis of foundation pit support structures such as continuous pile foundations or diaphragm walls, the planar elastic foundation beam model is commonly employed [41]. However, this model has inherent limitations for deep foundation pit engineering with pronounced spatial effects, as it struggles to accurately determine parameter values such as the foundation soil's horizontal resistance coefficient, base bed coefficient, spring compression stiffness, and support stiffness coefficient. By contrast, the multi-span cantilever beam model proposed herein can be solved using a superposition of simple material mechanics methods, while also accounting for additional loads acting on the bottom sealing structure.

The cofferdam foundation pit construction process reveals that steel pipe piles are first embedded into the stratum, followed by the placement of bottom sealing concrete within the steel pipe enclosure. The intimate contact between the steel pipe piles and bottom sealing, coupled with the differential water pressure inside and outside the cofferdam,

induces deformation of both components toward the free surface, thereby enhancing their compaction interaction. This mechanical behavior justifies simplifying the bottom sealing as a doubly fixed-end beam and the steel pipe piles as multi-span cantilever beams in the analytical model [36].

The construction technology and procedures for actual pier steel pipe pile cofferdams are highly complex, necessitating reasonable simplifications in both numerical and analytical approaches presented here. The theoretical derivation primarily addresses the deformation characteristics of steel pipe piles and bottom sealing during bottom-sealing construction, while numerical analysis shows that pile deformation prior to bottom-sealing construction is relatively minor, accounting for less than 10% of the total deformation. Although there are slight errors in the final deformation analysis and prediction of steel pipe piles, the research results retain substantial reference value for similar engineering applications.

This paper is a summary and sublimation of the previous research results. From the theoretical, it breaks through the internal mechanism of steel pipe pile and bottom sealing deformation in the construction process of cofferdam foundation pit excavation, dewatering and support, and the of cofferdam damage, that is, the principle of water bowl effect. For different soil and hydraulic conditions, our team has already studied the influence of various factors on the stress deformation of the cofferdam steel pipe pile through a large number of parameter sensitivity numerical simulation experiments in the early stage [37,38]. Mainly including the spatiotemporal evolution effect of steel pipe pile and bottom sealing in the construction process of cofferdam foundation pit excavation, dewatering and support, the deformation characteristics of steel pipe pile and bottom sealing under homogeneous and layered geological conditions the influence law of stratum strength characteristics on steel pipe pile and bottom sealing deformation, the seepage characteristics and anti-seepage effect of thin soil intercalation distribution in theum, and the influence mechanism of the relative position relationship of thin soil intercalation-bottom sealing-steel pipe pile on steel pipe pile and bottom sealing deformation. The feasibility of thin soil intercalation as cofferdam bottom sealing and other issues.

The uplift deformation of the cofferdam bottom sealing is influenced not only by buoyancy from differential water pressure but also significantly by additional horizontal loads induced by the water pressure difference inside and outside the foundation pit (trans: differential water pressure inside and outside the foundation pit). When analyzing structure deformation and damage caused by the “water basin effect,” focusing solely on vertical buoyancy is insufficient; the squeezing effect of lateral basin-side loads must also be considered.

The theoretical model of this article is derived based on the homogeneous strata and hydrostatic pressure, which are the dominant load conditions in engineering construction. For the occasional load impact of dynamic loads such as floods [17] and earthquakes, it is necessary to conduct specialized research, but it can be temporarily not considered. The article mainly aims at the relatively homogeneous stratum, relatively simple load, and relatively regular shape of the piererdam foundation pit, and the applicability of the relevant analytical results is relatively good and has general validity. However, for large-scale or complex cofferdam projects such as complex stratum distribution, large cofferdam foundation pit groups, or even diversion tunnel cofferdam and dam cofferdam [12], modifications or further research are required. And the theoretical model mainly considers the characteristic water–soil load changes that the steel pipe pile is subjected to the influence of the excavation of the riverbed stratum, start and stop of dewatering within the cofferdam, and the construction of support such as the diaphragm and horizontal bracing, etc., and the actualerdam construction process is simplified into four main stages, and then the

theoretical deduction of the evolution of the steel pipe pile's stress deformation is carried out by using the superposition principles.

This paper carries out the sublimation of theory and the mining of mechanism mainly based on the previous research. The research results of this are more generalizable. The main goal or core of this paper is to propose the principle of the water basin effect of the cofferdam foundation pit, to carry out the analytical derivation of the force deformation of the steel pipe pile-bottom seal under the condition of homogeneous soil layer and hydrostatic pressure. The expression contains the density, cohesion, and internal friction angle of the stratum, so for other strata, only the corresponding soil layer parameters need to be substituted, and the expression is equally applicable. For the layered strata, it is also only necessary to consider the soil pressure acting on the steel pipe pile according to the thickness of the layer. The main consideration of this paper is the of hydrostatic pressure inside and outside the cofferdam, and different water level conditions, the water level difference can be calculated according to the actual water level, and the expression is applicable. Therefore, the analytical derivation of this paper is generalizable.

6. Conclusions

This study introduces the water basin effect into the cofferdam foundation pits engineering. Based on the stress and deformation theoretical analysis of the simply supported beam under various loads, the evolution characteristics of the stress and deformation of the steel pipe pile and the bottom-seal are analyzed and derived by using the superposition method and the incremental method for four typical construction stages during the construction of the cofferdam. And the water basin effect mechanism and the evolution of steel pipe pile deformation in cofferdam foundation pits are systematically elucidated. Theoretical derivations are validated and applied through full-process hydrological–mechanical coupling simulation and in situ monitoring of the steel pipe pile cofferdam foundation pit for the 6# pier in Xi'an Metro Line 10's Jingwei River Rail-Shared Bridge. The main conclusions are as follows:

Water basin effect characterization: Under the combined action of the water basin effect and differential hydro-sedimentary pressures across the cofferdam boundary, the bottom seal exhibits heightened uplift susceptibility and potential anti-uplift failures even at relatively low hydraulic gradients.

Dewatering stage classification: The cofferdam dewatering process is systematically divided into four stages: Riverbed excavation for bottom sealing preparation. Dewatering to the elevation of the second internal support. Dewatering to the elevation of the third internal support. Final dewatering to the bottom sealing elevation.

Steel pipe pile model: The steel pipe pile structure is simplified as a single-span or multi-span cantilever continuous beam. Using the superposition principle, deformation evolution equations for this statically indeterminate structure are derived for each of the four construction stages, capturing the incremental load effects during dewatering.

Bottom sealing model: The bottom sealing concrete is modeled as a doubly fixed-end beam. By applying the principle of superposition, the deflection curve equation is established under combined actions of uniform vertical loads (self-weight, buoyancy) and end-fixed additional loads (differential water and soil pressures), providing a theoretical basis for deformation prediction.

Simulation validation: Full-process hydrological–mechanical coupling simulation of the actual cofferdam project confirms the deformation characteristics under the water basin effect. The steel pipe pile exhibits consistent "convex" horizontal deformation along the depth direction across all working conditions, with a trend of increasing first and then decreasing as construction progresses. At the main pier completion stage, the maximum

horizontal deformation of 20.72 mm occurs at 14 m below the pile top, showing good agreement with both analytical solutions and field measurements.

This paper mainly carries out the sublimation of theory and the mining of mechanism on the water basin effect, and the research results of this are more generalizable. The theoretical model of this article is derived based on the homogeneous strata and relatively simple load, and relatively regular shape, the applicability of the relevant analytical results is relatively good and has general applicability but for the occasional load or for large-scale or complex cofferdam projects, it is necessary to conduct specialized research modify or further. The next step can also attempt to break through the theoretical analysis of the water basin effect in terms of layered strata, fully continuous dynamic drain water, and simplification of pile-bottom contact supports.

Although simplifications were made in theoretical derivation and numerical modeling, the research results offer valuable insights into the deformation mechanisms of cofferdam structures under dewatering. These findings can serve as a reference for similar engineering projects involving deep foundation pits and water-retaining structures.

Author Contributions: Conceptualization, Q.Z., X.Z. and N.L.; methodology, N.L. and G.L.; software, N.L. and G.L.; validation, G.L., Q.Z., X.Z. and N.L.; formal analysis, N.L. and G.L.; investigation, G.L., Q.Z., X.Z., N.L. and Y.H.; writing—original draft preparation, G.L. and Y.H.; writing—review and editing, G.L., N.L. and Y.H.; supervision, G.L., Q.Z., X.Z. and N.L.; funding acquisition, G.L. and N.L. All authors have read and agreed to the published version of the manuscript.

Funding: The authors would like to acknowledge the following financial supports: Project (52309144, 52179111) supported by National Natural Science Foundation of China, Project (GZC20232139, 2024M762626) supported by China postdoctoral researchers funded planning and China Postdoctoral Science Foundation, Project (KY202106) supported by Shaanxi Geological Mining Group Co., Ltd. scientific research special fund.

Institutional Review Board Statement: Not applicable.

Informed Consent Statement: Not applicable.

Data Availability Statement: The data used to support the findings of this study are available from the corresponding author upon request.

Acknowledgments: We would like to thank the anonymous reviewers for their time and effort devoted to improving the quality of this research. The financial support provided by this sponsor is greatly appreciated.

Conflicts of Interest: Authors Qinchao Zuo and Xiaoyan Zhou were employed by the company Shaanxi Institute of Engineering Investigation Co., Ltd. The authors declare that this study received funding from Shaanxi Geological Mining Group Co., Ltd. The funder was also involved in the study design, collection, analysis, interpretation of data, the writing of this article or the decision to submit it for publication.

References

1. Kang, Y.; Zhang, W.; Li, P.; Hao, D.; Wan, C.; Miao, C. Construction of Long-Span Bridge Bearing Platforms in Deep and Thick Silt Interlayers. *Adv. Civ. Eng.* **2024**, *2024*, 6796743. [CrossRef]
2. Li, D.S.; Yang, K.C.; Zhou, S.W. Effect of Residual Cofferdam at the Diversion Tunnel Inlet on the Index of River Closure and the Dumped Materials: A Case Study. *Ain Shams Eng. J.* **2022**, *13*, 101616. [CrossRef]
3. Uribe-Henao, A.F.; Arboleda-Monsalve, L.G.; Aguirre-Molina, D.A.; Zapata-Medina, D.G. Construction-Induced Effects in a Cofferdam Excavation Using Hypoplasticity and Shotcrete Models. *Tunn. Undergr. Space Technol.* **2022**, *124*, 104446. [CrossRef]
4. Jiang, Z.; Yang, C.; Yue, H. Multi-Objective Optimization of Steel Pipe Pile Cofferdam Construction Based on Improved Sparrow Search Algorithm. *Appl. Sci.* **2024**, *14*, 10407. [CrossRef]

5. Xu, G.; Jiang, Z.; Zhou, J.; Xu, L.; Liao, Z.; Xu, Y. Hydrodynamic Optimization and Performance Verification of Fairings for Round-Ended Cofferdams Using Dam-Break Wave Experiments and Numerical Simulations. *Appl. Ocean Res.* **2024**, *153*, 104247. [CrossRef]
6. Liu, A.; Li, B.; Chen, J.; Gao, C. Research and Application of Large Diameter Steel Cylinder Island Construction Technology in Hong Kong-Zhuhai-Macao Bridge Project. *Ships Offshore Struct.* **2020**, *15*, 727–738. [CrossRef]
7. Zhu, Y.; Bi, J.; Xing, H.; Peng, M.; Huang, Y.; Wang, K.; Pan, X. Stability Analysis of Cofferdam with Double-Wall Steel Sheet Piles under Wave Action from Storm Surges. *Water* **2024**, *16*, 1181. [CrossRef]
8. Yuan, F.; Chen, W. Stability Analysis of Temporary Cofferdam of a Ship Lock Construction Project in Coastal Area. *IOP Conf. Ser. Earth Environ. Sci.* **2021**, *768*, 012118. [CrossRef]
9. Wang, K.; Gao, Y.; Jin, Z.; Zhou, X.; Chen, L.; Zhang, C. Research on Stability of Steep Bank Slope and Reserved Thin-Walled Rock Cofferdam during Excavation of Intake Foundation Pit. *Eng. Fail. Anal.* **2022**, *141*, 106659. [CrossRef]
10. Xie, D.; Li, X.; Zhou, T.T.; Feng, Y.Q. Estimating the Contribution of Environmental Variables to Water Quality in the Postrestoration Littoral Zones of Taihu Lake Using the APCS-MLR Model. *Sci. Total Environ.* **2022**, *857*, 159678. [CrossRef]
11. Erdem, E.; Kolay, E.; Yildirim, F.; Çadir, C.C. The Investigation of the Seepage Condition of an Upstream Cofferdam with Computer Simulations and Field Observations (the Case Study: Inandik Dam-Turkey). *Environ. Earth Sci.* **2024**, *83*, 583. [CrossRef]
12. Li, F.; Huang, J. Deformation Law and Stability State of Cofferdam during Pumping Process in PC Combined Method Pile Cofferdam. *Desalinat. Water Treat.* **2023**, *313*, 315–330. [CrossRef]
13. Ti, Z.; Wei, K.; Qin, S.; Mei, D.; Li, Y. Assessment of Random Wave Pressure on the Construction Cofferdam for Sea-Crossing Bridges under Tropical Cyclone. *Ocean Eng.* **2018**, *160*, 335–345. [CrossRef]
14. Wang, X.; Que, Y.; Wang, K.; Diao, H.; Cui, Y.; Li, Q. A Field Test Scrutiny on Bearing Mechanism of Super-Long Bored Piles in Deep Fine Silty Sand Layers. *Mar. Georesources Geotechnol.* **2023**, *41*, 162–174. [CrossRef]
15. Wang, Q.; Li, C.; Ma, Y.; Hu, Z.; Lv, H.; Liu, W. Research on Deformation Characteristics and Design Optimization of Super-Large Cofferdam Enclosure Structure. *Buildings* **2023**, *13*, 2429. [CrossRef]
16. Hermansyah, H.; Irwan, I.; Satria, H.; Dayana, I.; Salam, R. Simulation of Cofferdam Calculations Using Geo-Studio Application in Peusangan Hydropower Dam Construction. *Andalasian Int. J. Appl. Sci. Eng. Technol.* **2023**, *3*, 89–92. [CrossRef]
17. Jiang, P.; Huang, Y.; Tao, Z.; Zhu, J.; Wang, N.; Qiao, J. Deformation Characteristics and Safety Evaluation of the Throw Filling Soft Clay Cofferdam under Super-Historical Flood Conditions. *Adv. Civ. Eng.* **2022**, *2022*, 9578477. [CrossRef]
18. Ayiheng, H.; Cheng, J.; Pan, J.; Zhang, L. Study on Slope Stability and Reinforcement Measures of an Earth-Rock Cofferdam on Deep Overburden Foundation. *IOP Conf. Ser. Earth Environ. Sci.* **2019**, *218*, 012004. [CrossRef]
19. Kai, C.; Xu, J. Mechanical Properties of Sheet Pile Cofferdam during Adjacent Open Cut Tunnel Construction near Lake Bottom. *Appl. Sci.* **2023**, *13*, 6191. [CrossRef]
20. Chen, S.; Wang, Y.; Li, Y.; Li, X.; Guo, P.; Hou, W.; Liu, Y. Deformation and Force Analysis of Wood-Piled Island Cofferdam Based on Equivalent Bending Stiffness Principle. *Buildings* **2022**, *12*, 1104. [CrossRef]
21. Osthoff, D.; Grabe, J. Deformational Behaviour of Steel Sheet Piles during Jacking. *Comput. Geotech.* **2018**, *101*, 1–10. [CrossRef]
22. Li, C.; Ding, X.M.; Wang, Z. Anti-Sliding Mechanism of Soil-Rock Slope in Transparent Soil and Discrete-Element Method. *Int. J. Phys. Model. Geotech.* **2021**, *21*, 186–195. [CrossRef]
23. Shen, Y.; Yu, Y.; Ma, F.; Mi, F.; Xiang, Z. Earth Pressure Evolution of the Double-Row Long-Short Stabilizing Pile System. *Environ. Earth Sci.* **2017**, *76*, 476. [CrossRef]
24. Hui, S. Research on the Bearing Capacity of Double Row Steel Sheet Pile Reinforcement Depth of the Based on Soil between Piles. *Int. J. Eng. Res. Afr.* **2016**, *25*, 127–132. [CrossRef]
25. Lu, X.; Luo, Y.; Ming, H.; Zhou, M.; Zhang, X.; Liu, D. Stability of Nonuniform Large Geotextile-Reinforced Cofferdam under Seepage and Excavation Effects. *Int. J. Geomech.* **2023**, *23*, 04022283. [CrossRef]
26. Li, D.X.; Li, X.W.; Li, L.; Zhang, Q.Y. Effect of 2-D Spatial Variability of Soil Properties on Cofferdam Stability Considering Degradation of Soft Soil Foundation. *Bull. Eng. Geol. Environ.* **2024**, *83*, 248. [CrossRef]
27. Hu, Y.Q.; Huang, J.Y.; Tao, Z.P.; Zhu, J.H.; Lv, Q.; Qiao, J.W.; Cai, W.B. The Influence of Water-Level Fluctuation on the Instability and Seepage Failure of Dump-Fill Cofferdam. *Adv. Civ. Eng.* **2022**, *2022*, 5845340. [CrossRef]
28. Noh, J.; Lee, S.; Kim, J.-S.; Molinas, A. Numerical Modeling of Flow and Scouring around a Cofferdam. *J. Hydro-Environ. Res.* **2012**, *6*, 299–309. [CrossRef]
29. Chen, L.Y.; Jeng, D.S. Study on the Seabed Response around a Dumbbell Cofferdam under Combined Wave and Current Loading. *Ocean Eng.* **2022**, *256*, 111456. [CrossRef]
30. Wang, X.; Qu, K. Hydrodynamic Characteristics of Bridge Cofferdam Under Multidirectional Focused Waves. *J. Offshore Mech. Arct. Eng.* **2024**, *146*, 061202. [CrossRef]
31. Chen, S.; Li, Y.; Guo, P.; Zuo, X.; Liu, Y.; Yuan, H.; Wang, Y. Ultimate Bearing Capacity of Bottom Sealing Concrete in Underwater Deep Foundation Pit: Theoretical Calculation and Numerical Analysis. *Machines* **2022**, *10*, 830. [CrossRef]

32. Xiao, B.; Zhu, K.W.; Xu, G.X.; Ye, H.X.; Chen, X.X. Structural Safety Analysis of Steel-Concrete Composite Single-Wall Caisson Cofferdams for Deep-Water Bridge Piers. *Soil Mech. Found. Eng.* **2024**, *61*, 469–475. [CrossRef]
33. He, P.; Zhang, H.; Zou, C. Antifloating fortification and control measures of "water basin effect". *J. Chongqing Univ.* **2022**, *45*, 25–29. [CrossRef]
34. He, Z.; Huang, J.; Yu, J.; Li, D.K.; Zhang, Z.Z.; Zhang, L. Analytical Solution for the Steady Seepage Field of a Circular Cofferdam in Nonhomogeneous Layered Soil. *J. Hydraul. Eng.* **2024**, *150*, 04024037. [CrossRef]
35. Madanayaka, T.; Sivakugan, N. Adaptation of Method of Fragments to Axisymmetric Cofferdam Seepage Problem. *Int. J. Geomech.* **2017**, *17*, 04017048. [CrossRef]
36. Xiong, C.; Tian, M.; Zhu, R.; Liu, N. Calculation and analysis of track bed floating characteristics of karst tunnel considering water basin effect. *J. Guizhou Univ.* **2024**, *41*, 63–70. [CrossRef]
37. Li, G.; Kang, Z.; Zhou, X.; Zhang, X.; Yan, Z.; Li, N. Water basin effect and influencing mechanism of cofferdam foundation pit. *J. Chang. Univ. Sci. Technol.* **2025**, *22*, 61–77. [CrossRef]
38. Li, Z.; Li, G.; Li, N. Study on the dewatering feasibility and water blocking effect of thin soil interlayer as the bottom layer of cofferdam. *Water Resour. Hydropower Eng.* **2024**, *55*, 69–80. [CrossRef]
39. Sun, X.; Fang, X.; Guan, L. *Mechanics of Materials*; Higher Education Press: Beijing, China, 2019.
40. Wang, Z.; Shi, W.; Jiang, K.; Yu, F.; Xiong, H.; Ai, X. Coupling Analysis of Stress Field and Seepage Field in Foundation Pit Dewatering and Optimization Design of Reinjection. *Therm. Sci. Eng. Prog.* **2024**, *54*, 102778. [CrossRef]
41. Wei, H.; Wang, P.; Zheng, X. Analytical and Numerical Investigation of Internal Force Distribution in "Pile-Wall" Structures Based on Finite Difference Method. *Building* **2025**, *15*, 1455. [CrossRef]